JOURNAL OF MAGNETIC RESONANCE **129,** 10–18 (1997)
ARTICLE NO. MN971251

Quadrupolar Relaxation of Spin 3 in the Intermediate $\omega_0\tau_c$ Regime

A. Baram* and P. Bendel†

*Soreq NRC, Yavne 81800, Israel; and †Department of Chemical Services, MR Center, The Weizmann Institute of Science, Rehovot 76100, Israel

Received April 7, 1997

The equations for the quadrupolar relaxation of spin 3 were derived for the Redfield limit where the molecular reorientation rate is much faster than the size of the quadrupolar interaction. In the extreme narrowing regime ($\omega_0\tau_c \ll 1$), the results converge to the analytical expressions for the relaxation rates available in the literature. For slower motions, both longitudinal (spin–lattice) and transverse (spin–spin) relaxations are described by a superposition of three exponentials, where both the rates themselves and their relative weights are functions of $\omega_0\tau_c$. Numerical calculations of the relevant relaxation parameters in the intermediate $\omega_0\tau_c$ regime are presented. Spin–lattice relaxation is described to very good approximation by a single exponential for all values of $\omega_0\tau_c$, with the weight of the dominant decay mode exceeding 0.97 for the entire range. The predictions of these simulations were found to be in good agreement with experimentally measured relaxation rates of the ^{10}B resonances in the sodium salt of $Na_2B_{12}H_{12}S$, mercaptoundecahydro-*closo*-dodecaborane (sodium borocaptate or BSH) dissolved in glycerol, determined at $\omega_0 = 53.73$ MHz, between temperatures of 268 and 323 K. The fit to the experimental results yielded a value of 1.25 MHz for the average ^{10}B quadrupolar coupling constant in this molecule.

INTRODUCTION

It is well known that the quadrupolar interaction causes phenomena such as nonexponential relaxation (*1, 2*) and dynamic frequency shifts (*3, 4*), for nuclear spins ($I > \frac{1}{2}$) reorienting in liquids at a rate which is slower than defined by the extreme narrowing condition ($\omega_0\tau_c \ll 1$). Solutions and descriptions characterizing this behavior were derived mainly for half-integer spins, e.g., $\frac{3}{2}$ (*1*), $\frac{5}{2}$, and $\frac{7}{2}$ (*2–5*). A solution for spin 3 was not yet derived, possibly because only a single nucleus in the periodic table (^{10}B) possesses this spin quantum number. There is, however, some interest in characterizing the relaxation properties of the ^{10}B nucleus, due to its necessary appearance in molecules used in a form of cancer treatment known as boron neutron capture therapy (BNCT) (*6*). In this treatment, it is very important to conduct the neutron irradiation at a time at which the ratio between the concentrations of the boronated molecule in the tumor and in the blood is maximized, and to know the ^{10}B concentrations for dosimetry planning. There is currently no method for noninvasive monitoring of ^{10}B-containing molecules, so that MRI or localized NMR spectroscopy can make a significant contribution to the clinical implementation of BNCT. Since biological environments can impose motional restriction on these ^{10}B-labeled molecules, a quantitative understanding of ^{10}B relaxation under such conditions is important for both direct and indirect detection of the ^{10}B spins (*7–10*).

THEORY

Spin–Spin Relaxation

The Hamiltonian for the quadrupolar interaction can be written as

$$H_Q = \frac{3e^2qQ}{4I(2I-1)} \times \left[I_z^2 - \frac{1}{3} I(I+1) + \frac{\eta}{6}(I_+^2 + I_-^2) \right], \quad [1]$$

where e^2qQ is the quadrupolar coupling constant (qcc), η is the asymmetry parameter of the electric field gradient (EFG) tensor, and I_+ and I_- are the usual raising and lowering operators. The spin operators are defined in the laboratory principal axes, while the EFG tensor components are defined in the molecular frame of reference. Substituting the value for $I = 3$, and converting the Hamiltonian to units of hertz, one obtains

$$H_Q = \frac{\pi(qcc)}{10} \left[I_z^2 - \frac{1}{3} I(I+1) + \frac{\eta}{6}(I_+^2 + I_-^2) \right]. \quad [2]$$

This Hamiltonian is mathematically identical to the Hamiltonian describing the zero-field splitting (ZFS) interaction in ESR (*3, 4*). As long as the absolute size of the quadrupolar interaction (which is of the order of qcc) is small compared to the modulation rate of this interaction (which is of the order of the molecular correlation rate τ_c^{-1}), the longitudinal and transverse relaxation properties can be derived through Redfield's relaxation matrix **R** (*11*). The real (R^r)

1090-7807/97 $25.00

and imaginary (R^{i}) parts of each matrix element can be calculated through (*4*)

$$R^{r}_{aa'bb'} = 2J_{aba'b'}(\omega_{ab}) - \delta_{ab}\sum_{c}[J_{acbc}(\omega_{bc}) + J_{cacb'}(\omega_{cb'})] \quad [3]$$

$$R^{i}_{aa'bb'} = -\delta_{ab}\sum_{c}[K_{acbc}(\omega_{bc}) + K_{ca'cb'}(\omega_{cb'})], \quad [4]$$

where

$$J_{aba'b'}(\omega_{ab}) = c'j[(a-b)\omega_0]\langle a|T^{2p}|b\rangle\langle a'|T^{2p}|b'\rangle^* \quad [5]$$

$$K_{aba'b'}(\omega_{ab}) = c'p\omega_0\tau_c j[(a-b)\omega_0]\langle a|T^{2p}|b\rangle\langle a'|T^{2p}|b'\rangle^*, \quad [6]$$

where * denotes the complex conjugate and c' is a constant given in our case by

$$c' = \frac{\pi^2(qcc)^2(1+\eta^2/3)}{750}. \quad [7]$$

The spectral densities are defined as

$$j(n\omega_0) = j_n = \frac{\tau_c}{1+(n\omega_0\tau_c)^2}. \quad [8]$$

The indices a, b, c, a', and b' run over the states from -3 to $+3$, and $p = a - b$. T^{2p} are the spin operators as defined in Ref. (*4*).

For spin–spin relaxation, the elements of **R** connect the allowed transitions in the energy level system, and are therefore calculated only for $a = a' - 1$ and $b = b' - 1$. For spin I, there are $2I$ allowed transitions, and the rank of **R** is in principle $2I$. However, the symmetry of these transitions around the unperturbed Zeeman energy ω_0 suggests that the dimensionality of the problem should be reducible to rank I (or $I + \frac{1}{2}$ for half-integer spins). Based on the inversion invariance of the full matrix **R** ($R_{aa'bb'} = R_{-b'b-a'a}$), and the reflection invariance of the vector representation of the operator I_+, i.e., $(I_+)_{aa'} = (I_+)_{-a'-a}$, we can define a reduced 3×3 relaxation matrix $\mathbf{R}'$, which governs the evolution of a reduced density vector ρ',

$$\frac{d\rho'}{dt} = \mathbf{R}'\rho', \quad [9]$$

where the elements of ρ' are defined as symmetric combinations ρ:

$$\rho' = \frac{1}{2}\begin{pmatrix}\rho_{32}+\rho_{-2-3}\\ \rho_{21}+\rho_{-1-2}\\ \rho_{10}+\rho_{0-1}\end{pmatrix}. \quad [10]$$

Performing the calculations as prescribed in Eqs. [3]–[6] leads to

$$\mathbf{R}'_2 = 5c'\begin{pmatrix}A & B & C\\ B & D & E\\ C & E & F\end{pmatrix}, \quad [11]$$

where

$$A = -\left(\frac{15}{2}j_0 + \frac{39}{2}j_1 + 9j_2\right) - i\omega_0\tau_c\left(\frac{21}{2}j_1 - 6j_2\right) \quad [12a]$$

$$B = 3\sqrt{15}j_1 \quad [12b]$$

$$C = 6\sqrt{2}j_2 \quad [12c]$$

$$D = -\left(\frac{27}{10}j_0 + \frac{171}{10}j_1 + \frac{81}{5}j_2\right) - i\omega_0\tau_c\left(\frac{9}{10}j_1 + \frac{18}{5}j_2\right) \quad [12d]$$

$$E = \frac{3\sqrt{30}}{5}(j_1 + 4j_2) \quad [12e]$$

$$F = -\left(\frac{3}{10}j_0 + \frac{15}{2}j_1 + \frac{111}{5}j_2\right) + i\omega_0\tau_c\left(\frac{39}{10}j_1 - \frac{42}{5}j_2\right). \quad [12f]$$

The elements in $\mathbf{R}'_2$ are identical to those in the full Redfield matrix, except for

$$E = R_{-2-1-10} + R_{-2-101} \quad [13a]$$

and

$$F = R_{-10-10} + R_{-1001}. \quad [13b]$$

The relaxation matrix $\mathbf{R}_2$ is a complex symmetric matrix, with a spectrum of complex eigenvalues. However, at both limits ($\omega_0\tau_c \ll 1$ and $\omega_0\tau_c \gg 1$) its imaginary part is negligible. Furthermore, at the limit $\omega_0\tau_c \gg 1$, the nonsecular contributions are negligible and the matrix converges to a diagonal form.

The time-domain signal of the transverse magnetization consists of a superposition of three exponentially decaying components for which the weights (amplitudes) and decay rates can be calculated through the eigenvalues and eigenvectors of $\mathbf{R}'_2$. Let λ_j and $\boldsymbol{\xi}_j$ be the jth eigenvalue and eigen-

vector, respectively, and let $\mathbf{S}_+$ be the normalized vector representation of I_+, with components

$$\mathbf{S}_+ = \sqrt{3/14}, \sqrt{5/14}, \sqrt{6/14}; \quad [14]$$

then the weight of each of the three decaying exponentials is the square of the scalar product,

$$W_{2,j} = (\mathbf{S}_+ \cdot \boldsymbol{\xi}_j)^2, \quad [15]$$

the relaxation rates are

$$\frac{1}{T_2^j} = -\lambda_j^{\mathrm{r}}, \quad [16]$$

and the second-order dynamic frequency shifts (in Hz) are

$$\delta\nu_j = \lambda_j^{\mathrm{i}}/2\pi, \quad [17]$$

where the superscripts i and r refer to the imaginary and real parts of the respective eigenvalues.

Spin–Lattice Relaxation

Here the matrix elements connect the populations of the different energy levels, i.e., $a = a'$ and $b = b'$. The full Redfield matrix should therefore consist of 7×7 elements, but symmetry considerations again allow the calculation of the relaxation rates through a reduced matrix of size 3×3. This is due to the fact that the energy levels can be seen as being arranged in three pairs ($m_z = \pm 1, \pm 2, \pm 3$) symmetrically around the center level ($m_z = 0$), the absolute energy of which is irrelevant. In other words, the operator I_z is antisymmetric with respect to reflection, and the trace of the density matrix is time invariant. The reduced matrix for T_1 relaxation again fulfills Eq. [9], but the density matrix elements are now given by

$$\rho = \frac{1}{2}\begin{pmatrix} \rho_{33} - \rho_{-3-3} \\ \rho_{22} - \rho_{-2-2} \\ \rho_{11} - \rho_{-1-1} \end{pmatrix}. \quad [18]$$

The reduced Redfield matrix has the same form as in Eq. [11], with the elements given by

$$A = -(15j_1 + 6j_2) \quad [19a]$$

$$B = 15j_1 \quad [19b]$$

$$C = 6j_2 \quad [19c]$$

$$D = -(24j_1 + 12j_2) \quad [19d]$$

$$E = 9j_1 \quad [19e]$$

$$F = -(51j_1 + 174j_2)/5. \quad [19f]$$

As expected, the matrix $\mathbf{R}_1$ is a real symmetric matrix for all values of $\omega_0\tau_c$, and its eigenvalues are real. The matrix is free of secular contributions, and as a result the off-diagonal elements are comparable to the diagonal elements for all values of $\omega_0\tau_c$. In the $\omega_0\tau_c \gg 1$ limit the matrix elements (and its eigenvalues) are of the order of $(\omega_0^2\tau_c)^{-1}$. The function describing the relaxation of the longitudinal magnetization consists of three exponentials with rates corresponding to the three eigenvalues of the above matrix,

$$\frac{1}{T_1^j} = -\lambda^j, \quad [20]$$

and the weights of each component are given by the scalar product

$$W_{1,j} = (\mathbf{S}_z \cdot \boldsymbol{\xi}_j)^2, \quad [21]$$

where the vector $\mathbf{S}_z$ has components

$$\mathbf{S}_z = 1/\sqrt{14}, 2/\sqrt{14}, 3/\sqrt{14}. \quad [22]$$

SIMULATIONS

Extreme Narrowing Limit

In the extreme narrowing limit ($\omega_0\tau_c \ll 1$), the spectral densities j_n are n-independent, and they converge to their limiting value τ_c. In addition, the imaginary part of the transverse relaxation matrix $\mathbf{R}_2'$ is of order $O(\tau_c^2)$, negligible compared to its real part. Both relaxation matrices are real symmetric matrices in this regime. Furthermore, it is easy to see that the matrices become similar, with identical spectra of eigenvalues. In both cases, the eigenvector $\boldsymbol{\xi}_3$ corresponding to the largest eigenvalue λ_3 (recall that the eigenvalues are all negative) is identical to the characteristic weight vector, $\mathbf{S}_+$ or $\mathbf{S}_z$, of the relaxation process. The two additional eigenvectors (in each case) are orthogonal to the characteristic weight vector, and as a result the weights of their decaying exponentials vanish. Thus, both T_1 and T_2 appear single-exponential, with the eigenvalues approaching the well-known analytical result (*11*)

$$-\lambda_3 = 45c'\tau_c = \frac{1}{T_1} = \frac{1}{T_2} = \frac{3\pi^2(2I+3)(qcc)^2(1+\eta^2/3)\tau_c}{10I^2(2I-1)}. \quad [23]$$

When the condition for the extreme narrowing approximation is no longer fulfilled, the relaxation of the transverse

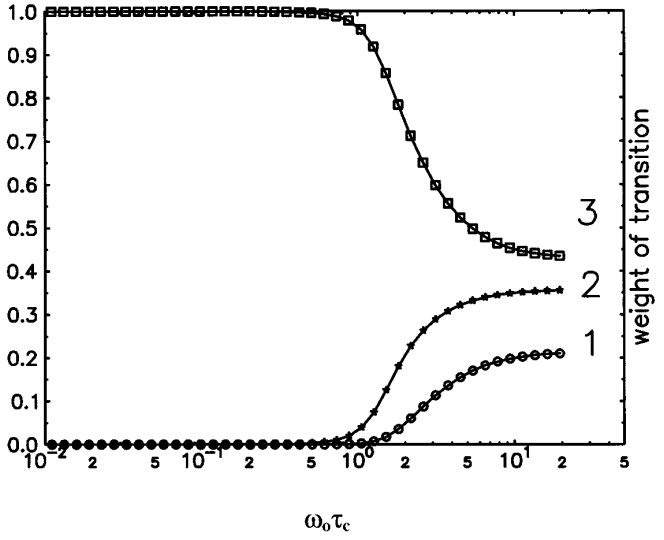

FIG. 1. Relative weights for each of the three transverse relaxation components ($W_{2,j}$), for $j = 1, 2, 3$, as indicated on the right side of the plot.

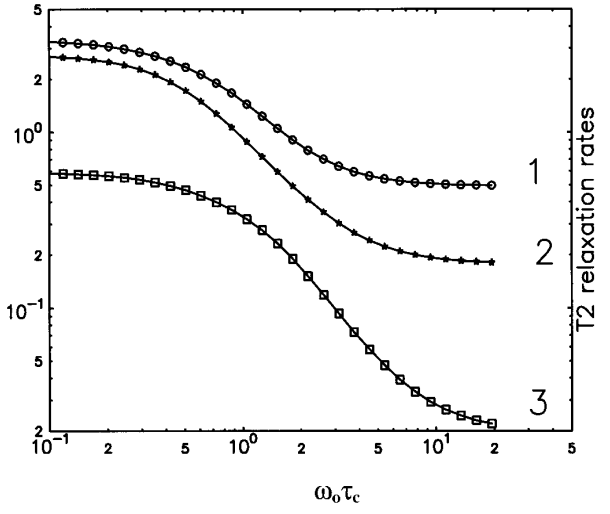

FIG. 2. Relaxation rates for each of the three transverse relaxation components for $j = 1, 2, 3$, as indicated on the right side of the plot. The vertical scale is in units of $(qcc)^2\tau_c$.

magnetization (M_t), following excitation by a 90° pulse, is given by

$$M_t(t) = M_0 \sum_{j=1}^{3} W_{2,j}\exp(-t/T_2^j), \qquad [24]$$

where M_0 is the equilibrium magnetization. The corresponding equation describing the recovery of the longitudinal magnetization (M_z), following inversion by a 180° pulse, is

$$M_z(t) = M_0[1 - 2\sum_{j=1}^{3} W_{1,j}\exp(-t/T_1^j)]. \qquad [25]$$

Spin–Spin Relaxation and Dynamic Frequency Shifts

As long as the second-order dynamic frequency shifts are small compared to the linewidths, and relaxation is predominantly determined by one of the three modes, it is more natural to describe the system through analysis of the transverse relaxation, rather than apply the full lineshape calculation. In all the calculations presented in this section the effective quadrupole coupling constant is the product $(qcc)\sqrt{1 + \eta^2/3}$.

Figure 1 displays the relative weights ($W_{2,j}$) of the three components contributing to T_2 relaxation, as function of $\omega_0\tau_c$. As expected, one of the amplitudes ($W_{2,3}$) dominates in the extreme narrowing limit. From about $\omega_0\tau_c \approx 1$, the amplitudes gradually converge, reaching the asymptotic values of 6/14, 5/14, and 3/14 at $\omega_0\tau_c \gg 1$. These values correspond to the relative intensities of the relevant transitions in the solid-state spectrum.

The values of the exponential relaxation rates for each of the three transitions are displayed in Fig. 2, in units of $(qcc)^2\tau_c$. As evident from the graph, the dominant mode also relaxes at the slowest rate. The graphs in Fig. 3 illustrate the results of the calculation for the case of a quadrupolar coupling constant of 1.25 MHz, and a field strength of 11.75 T, for which the ^{10}B resonance frequency is 53.73 MHz. The expected linewidths (full width at half-intensity) and second-order dynamic frequency shifts of the dominant transition are shown as a function of τ_c. The maximum–minimum of the linewidth and the sign inversion of the dynamic shift are results of the third-order solution for the eigenvalues, and are not encountered for lower quadrupolar spins.

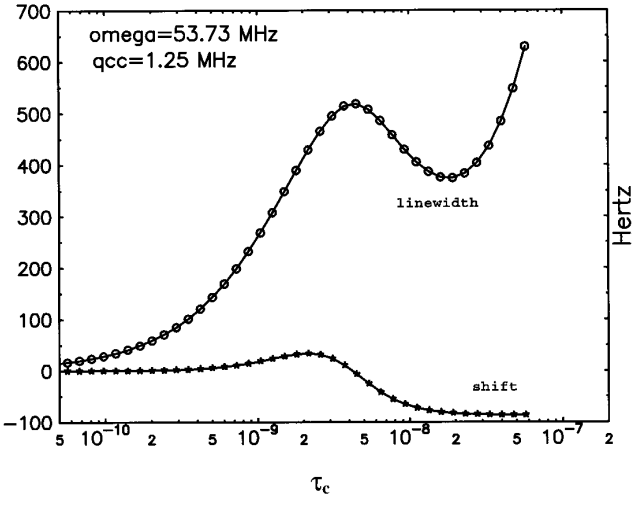

FIG. 3. Linewidth at half-intensity, and dynamic frequency shift for the dominant $j = 3$ relaxation mode, calculated for $\nu_0 = 53.73$ MHz and $qcc = 1.25$ MHz.

Spin–Lattice Relaxation

The calculation of the weights for the T_1 relaxation components revealed that the amplitude of the $j = 3$ component (which corresponds to the symmetric combination of the populations) completely dominates for the entire range of $\omega_0\tau_c$ values which are still amenable to the Redfield formalism, using realistic values for the Larmor frequency and typical ^{10}B quadrupolar coupling constants. In fact, the weight of this component asymptotically approaches a value of 0.97, with the other two components contributing only about 3% to the spin–lattice relaxation. Therefore, for the practical purpose of predicting and evaluating ^{10}B relaxation at intermediate $\omega_0\tau_c$ values, the T_1 process can be considered single-exponential, with a rate corresponding to the λ_3 eigenvalue.

Approximate Solutions

Halle and Wennerström (*12*) suggested the use of the eigenvectors obtained for the extreme narrowing limit as a basis for an approximation to the relaxation rates for slower motions. Their approach results in single approximate relaxation rates for T_1 and T_2. In our case, the corresponding eigenvectors are given in Eqs. [14] and [22]. The approximate relaxation rates derived are

$$\left(\frac{1}{T_2}\right)_{\text{appr}} = \frac{9}{2}\,c'(3j_0 + 5j_1 + 2j_2) \qquad [26]$$

$$\left(\frac{1}{T_1}\right)_{\text{appr}} = 9c'(j_1 + 4j_2). \qquad [27]$$

Figure 4 displays the λ_3 eigenvalues derived from the exact calculations for spin–lattice and spin–spin relaxation, and also the approximate solutions by Eqs. [26] and [27]. One sees that indeed, as long as one relaxation component dominates, the approximate and exact solutions are very close. This is fulfilled for T_1 over the entire range, but breaks down for T_2 around $\omega_0\tau_c \approx 1$.

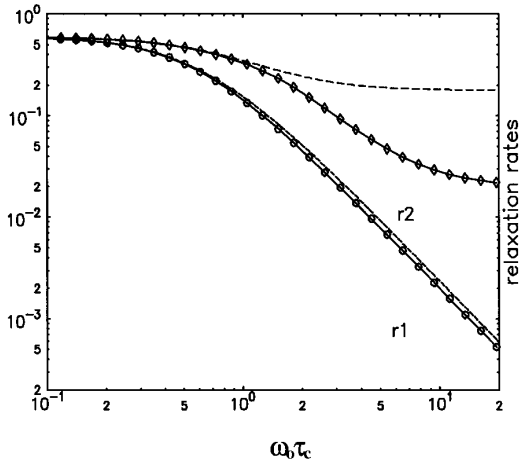

FIG. 4. Longitudinal (r1, circles) and transverse (r2, diamonds) relaxation rates of the dominant $j = 3$ relaxation components, in units of $(qcc)^2\tau_c$. The dashed curves were calculated by the approximate solutions, Eqs. [26] and [27].

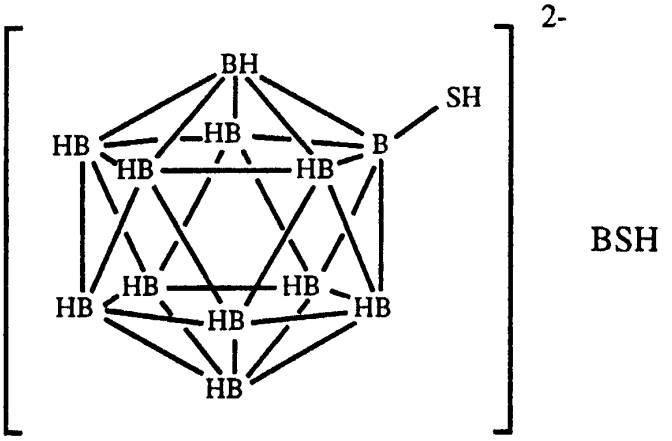

FIG. 5. Molecular structure of the mercaptoundecahydro-*closo*-dodecaborane (BSH) anion.

EXPERIMENTAL METHODS

^{10}B-enriched $Na_2B_{12}H_{12}S$ (BSH or sodium borocaptate, enrichment ≥95%) was purchased from Boron Biologicals (Raleigh, NC) and used without further purification. BSH was dissolved at 75 m*M* in glycerol. NMR experiments were performed on a Bruker DMX-500 NMR spectrometer (Karlsruhe, Germany), using a 10-mm broadband probe. The sample was contained in a quartz (boron-free) NMR tube, but the probe itself gave rise to a rapidly decaying background ^{10}B signal. It was verified that this signal decayed to below noise level (after 1000 scans) for a preacquisition ''dead'' time (DE) of 45 μs, which was then used in all the reported experiments (which all employed less than 1000 scans). T_1 experiments were performed using a standard inversion-recovery pulse sequence with 8–16 inversion delays; 180° pulse lengths were about 40 μs. The signal was easily visible in a single scan, but up to 80 averages were used (per inversion delay) to improve S/N. Signal intensities were measured on the Fourier-transformed spectra. Transverse relaxation was measured with CPMG echo trains (averaging up to 320 such echo trains) using delays of 200–700 μs between successive 180° pulses. Signal intensities were measured directly on the time-domain data. All data were acquired with a sampling rate of 5 μs between successive sampling points (SW = 200,000).

EXPERIMENTAL RESULTS AND DISCUSSION

A diagram of the molecular structure of the BSH anion is shown in Fig. 5. The four inequivalent boron sites can be

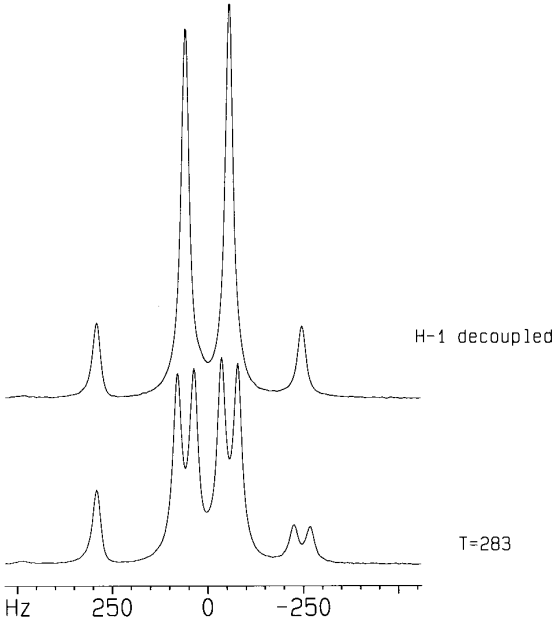

FIG. 6. Boron-10 NMR spectra (at 53.73 MHz) of 75 m*M* BSH dissolved in D_2O, at a temperature of 283 K. The upper trace spectrum was obtained with proton decoupling, while the lower trace spectrum shows the coupling to protons for 11 of the 12 boron atoms in the molecule. The spectra were acquired using a single scan (NS = 1), and displayed after exponential filter sensitivity enhancement using a 5-Hz line broadening (LB = 5).

distinguished on the ^{10}B NMR spectra of BSH dissolved in D_2O, shown in Fig. 6. Figure 7 shows, for comparison, the spectra of BSH in glycerol, at 323 and 273 K. The RF coil

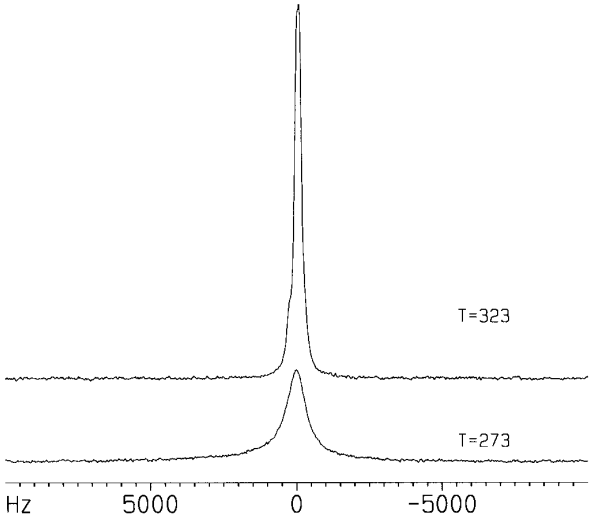

FIG. 7. ^{10}B spectra of 75 m*M* BSH dissolved in glycerol at temperatures of 323 K (upper trace) and 273 K (lower trace). Spectra were acquired and processed using NS = 1 and LB = 30. The relative integrated areas under the peaks are 1.00 for the spectrum at 323 K and 0.83 at 273 K.

TABLE 1
Experimentally Derived Parameters for ^{10}B Relaxation in BSH/Glycerol

Temperature (K)	$1/T_1$ (s^{-1})	$-\lambda_3$ (s^{-1})[a]	W_3[a]
268	299	1758	0.41
273	379	1718	0.50
278	483	1940	0.75
283	596	1920	0.90
288	685	1707	1.0
293	749	1475	1.0
298	764	1202	1.0
303	719	943	1.0
308	625	738	1.0
318	408	457	1.0
323	343	356	1.0

[a] $-\lambda_3$ is the apparent rate for the slowest component of transverse relaxation, and W_3 is the apparent weight of this component when extrapolated to $t = 0$.

and 90° pulse lengths were recalibrated at each temperature. The integrated peak areas for these two spectra were compared, in order to assess whether a significant fraction of the signal became ''invisible'' at the lower temperature. The peak at 273 K has an integral of 0.83 compared to the peak at 323 K. Taking into account an 18% increase in the equilibrium magnetization at the lower temperature (proportional to $1/T$), the relative ''visible'' signal fraction for BSH in glycerol at 273 K was 0.7. The 90° pulse length for these spectra was 29 μs, the preacquisition blanking delay 45 μs, and the sampling interval in each receiver channel 5 μs (the instrument used quadrature detection with sequential acquisition). Using the parameters derived below for the relaxation at 273 K according to our model (Table 2), one predicts a ''visible'' fraction of 0.85 for the above acquisition parameters. Given the uncertainties in determining the integrals of broad signals, and the true effective time of the signal sampling onset, there is reasonable agreement between the experimental observation and the theoretical expectation.

Table 1 lists the experimentally derived parameters for ^{10}B relaxation in BSH at various temperatures. Spin–lattice relaxation rates were determined from inversion-recovery experiments, and some of the data and their calculated fits are shown in Fig. 8. No deviation from single-exponential recovery could be detected in any of the data sets. It should be kept in mind that although the inequivalent boron sites may have different quadrupolar coupling constants and relaxation rates, they are not resolved on the BSH/glycerol spectra. Therefore all the results reported here, and the parameters derived from those results, represent averages which are probably heavily weighted toward the main-cage borons due to their large contribution (10/12) to the total spectral intensity.

For all temperatures between 288 and 323 K, the transverse relaxation rates reported in Table 1 were derived from the decay of echo centers on CPMG experiments. Some representative data sets are shown in Fig. 9. As a precaution, T_2 experiments were repeated using different values for the interecho delays (2τ). In principle, erroneous apparent decay rates can be measured when the 2τ interval is too long (scalar couplings, exchange, diffusion, off-resonance effects) or when it is too short (spin locking). In the first case (i.e., 2τ too long), the apparent T_2 values will usually underestimate the true values (i.e., the apparent decay will be faster than the true decay), while in the second case the apparent T_2 should be longer than the true value. In the temperature range indicated above, no significant changes in the measured T_2 values were observed for variations of 2τ between 0.2 and 0.7 ms. However, for the lower temperatures (268–283 K), we observed a systematic variation of the apparent decay rates with 2τ, but in a direction which was opposite from that expected according to the above considerations: the relaxation rates became *slower* with increasing interecho delays. We have, at this point, no explanation for the above phenomenon, and can only speculate that it may have something to do with the creation of multiple-quantum coherences by imperfect refocusing pulses. In any case, we decided to measure the slow-component T_2 values at the lower temperatures from the free induction decays (FIDs) as will be described in the following paragraph. These values were in all cases longer than the longest values determined by CPMG experiments, and are the ones listed in the first four rows of Table 1.

The magnitude of the free induction signal (i.e., the signal in both receiver channels added in quadrature) should decay according to the transverse relaxation rates (homogeneous broadening) and due to dephasing between isochromats with different resonance offsets (inhomogeneous broadening). The latter effect can be predicted exactly (neglecting magnetic field inhomogeneities) from the resolved spectrum measured in D_2O (Fig. 6), from which the weight and resonance offset of each isochromat can be determined. We calculated this ''inhomogeneous decay'' function, and then divided the experimental magnitude FIDs at the four lowest temperatures by this function, to obtain a ''corrected'' FID, the decay of which should be given only by relaxation effects. An example of such a corrected FID is shown in Fig. 10, together with the exponential function that best fitted the decay at the later times, when only the signal from the slowest relaxation mode should contribute. The plots such as the one in Fig. 10 were also used to evaluate the apparent weights W_3, as listed in the last column of Table 1, by extrapolating the curves back to $t = 0$. As can be seen, the apparent weight of the slow decaying component monotonically decreases with decreasing temperature, while the relaxation rate itself (third column in Table 1) goes through a maximum around 278 K, and then decreases with decreasing temperature.

The calculated values for various relaxation parameters, as implied by the theory, are listed in Table 2. These values were computed as follows: The maximal $1/T_1$ rate was estimated by interpolation to be $7.7 \times 10^2\ s^{-1}$. The simulated spin–lattice relaxation data predicts this $1/T_1$ maximum at $\omega_0\tau_c = 0.61$. Since the value of ω_0 is known, the value of the experimental $1/T_1$ maximum can then be used to calculate the quadrupolar coupling constant, which turned out to be 1.25 MHz (assuming an axially symmetric tensor). Using this value for qcc, the apparent values of τ_c were then calculated for all the temperatures, based on the best fit to the

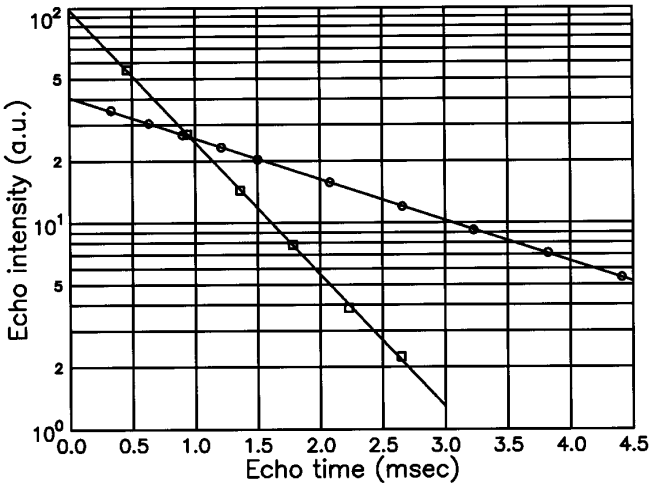

FIG. 9. Experimental results of CPMG echo-train experiments at 318 K (circles) with $2\tau = 250\ \mu s$ and at 293 K (squares) with $2\tau = 400\ \mu s$. The solid curves were calculated using decay rates of 457 s^{-1} for the 318 K and 1475 s^{-1} for the 293 K data.

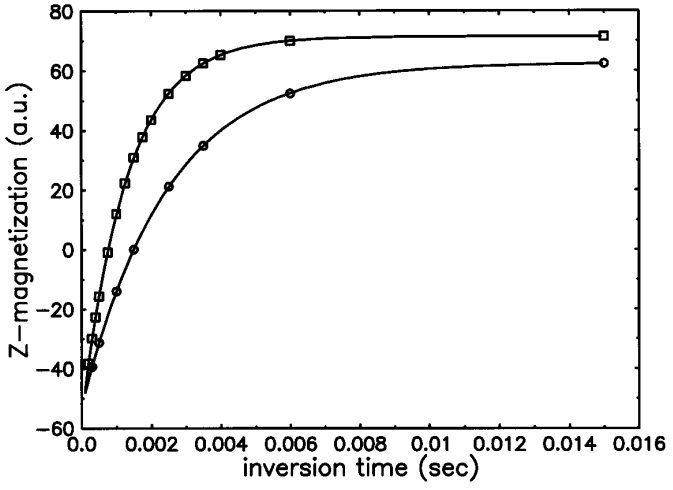

FIG. 8. Experimental results of inversion-recovery measurements at 308 K (circles) and at 298 K (squares). The solid curves were calculated using recovery rates of 408 s^{-1} for the 308 K and 764 s^{-1} for the 298 K data.

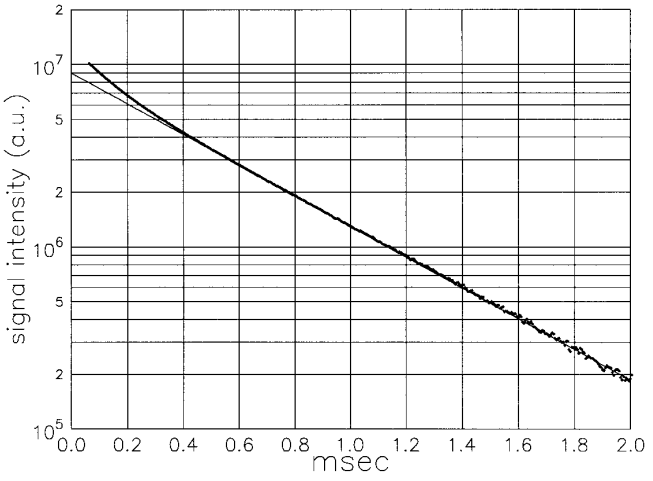

FIG. 10. The dots are the experimental magnitude FID points from the signal at 278 K, corrected for the first-order resonance offsets, as indicated in the text. The FID was acquired with 800 signal averages (repetition time = 100 ms). The solid line is the exponential fit with a decay rate of 1940 s^{-1}.

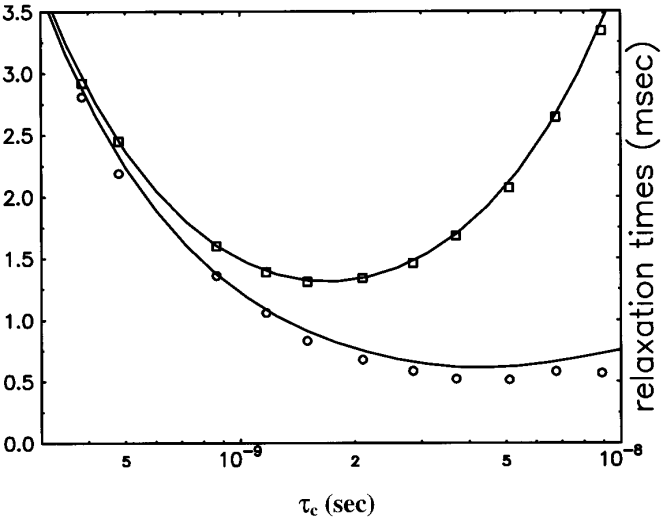

FIG. 11. Experimental T_1 relaxation times (squares) and slow components of T_2 relaxation times (circles) for ^{10}B in BSH/glycerol vs τ_c, which was set according to the best fit of the T_1 data to theory. The solid lines are the calculated curves, using a quadrupolar coupling constant of 1.25 MHz and a resonance frequency of 53.73 MHz.

experimental values of $1/T_1$. In case of deviation from axial symmetry this parameter will also incorporate the value of $(1 + \eta^2/3)$. Having thus set both *qcc* and τ_c for each temperature, all other parameters in Table 2, relating to spin–spin relaxation and dynamic frequency shifts, were calculated directly, without any further best-fit adjustments.

Figure 11 shows a graphical presentation of the experimental and calculated data, for T_1 and the dominant component of T_2 (λ_3). There is reasonably good agreement between the theory and the experimental behavior, although there is a tendency for the measured T_2 values to be shorter than the theoretically predicted values, for the lower temperatures where the faster transverse relaxation components become important. This trend is also reflected in the extrapolated apparent weights of the slow relaxation component, which are lower than predicted by the theory, using the values for τ_c as inferred from the T_1 values. It is possible that a contribution from $^1H-^{10}B$ dipolar interactions increases the measured relaxation rates. However, we cannot rule out that the experimental problems described before, i.e., the inability to measure very rapid transverse relaxation, and the error associated with the extrapolation to $t = 0$, introduced some systematic error into the reported transverse relaxation pa-

TABLE 2
Calculated Parameters for ^{10}B Relaxation in BSH/Glycerol

T(K)	τ_c[a]	$-\lambda_1$[b]	W_1[c]	$\Delta\delta_1$[d]	$-\lambda_2$[b]	W_2[c]	$\Delta\delta_2$[d]	$-\lambda_3$[b]	W_3[c]	$\Delta\delta_3$[d]
268	8.9	9153	0.107	378	4394	0.283	88	1386	0.61	−64
273	6.75	8122	0.07	334	4207	0.24	89	1518	0.69	−46
278	5.1	7583	0.03	275	4183	0.16	87	1622	0.81	−20
283	3.7	7259	0.007	199	4256	0.07	76	1627	0.92	12
288	2.85	6993	0.00	141	4345	0.03	64	1530	0.97	36
293	2.1				4330	0.009	50	1343	0.99	34
298	1.5							1105	1.00	29
303	1.17							930	1.00	22
308	0.865							733	1.00	14
318	0.48							433	1.00	5
323	0.385							352	1.00	3.5

[a] In nanoseconds.
[b] Transverse relaxation rates for the three components, in s^{-1}.
[c] Weights for the three transverse relaxation components.
[d] Second-order dynamic frequency shifts for the three components, in Hz.

rameters. In this region, the transverse relaxation should probably be measured with instrumentation having much shorter 90° and 180° pulses, shorter preacquisition ''dead times,'' and faster sampling rates.

We could not find any directly measured literature values of the boron quadrupolar coupling constants in BSH. The average ^{11}B *qcc* in BSH was recently estimated to be 0.8 MHz (*13*), based on concentration-dependent relaxation studies of BSH in protein solutions, using extrapolation to infinite dilution of BSH. This would imply a value of 1.6 MHz for ^{10}B, based on the ratio of quadrupole moments between the two isotopes, which does not necessarily contradict our present result, in view of the rather indirect nature of the ^{11}B measurements. Other published results on similar molecules include carboranes, $B_{10}C_2H_{12}$ (*14–16*), and decaborane, $B_{10}H_{14}$ (*17*). The values reported in (*14*) for the most symmetric boron sites imply ^{10}B *qcc* values as low as $\approx$1.5 MHz, but these measurements were later questioned by the subsequent reports (*15, 16*), which estimate the coupling constants for the same sites at about 2.3–2.5 MHz, and the values reported for decaborane are similar (*17*), i.e., much higher than indicated by the present measurements for the BSH anion. The common denominator for the comparison between BSH, carborane, and decaborane is the similar attachment of the Boron atoms to five other borons and a hydrogen. However, it is well known that the nominal covalent structural formulas are not sufficient to describe the actual bonding and charge distributions in boron hydrides (*18*). Since both carborane and decaborane are neutral molecules, while the BSH anion has a double negative charge, the resulting resonant structures could result in a more symmetric average environment for the boron atoms.

In summary, the theoretical equations for the relaxation of spin 3 in the intermediate $\omega_0\tau_c$ regime predict the following features, which were borne out by experimental measurements: (a) The spin–lattice relaxation remains practically single exponential. (b) The spin–spin relaxation is dominated by a single component with the slowest relaxation rate up to $\omega_0\tau_c \approx 1$. As the motion becomes slower, the rate of this relaxation component goes through a maximum, while its weight decreases, and the weights of the more rapid relaxation modes increase, so that the transverse relaxation decay becomes distinctly nonexponential.

ACKNOWLEDGMENTS

This research was supported by a grant from the U.S.–Israel Binational Science Foundation (BSF), Jerusalem, Israel. We thank one of the referees for drawing our attention to Ref. (*12*).

REFERENCES

1. P. S. Hubbard, *J. Chem. Phys.* **53,** 985 (1970).
2. M. Rubinstein, A. Baram, and Z. Luz, *Mol. Phys.* **20,** 67 (1971).
3. A. Baram, Z. Luz, and S. Alexander, *J. Chem. Phys.* **58,** 4558 (1973).
4. R. Poupko, A. Baram, and Z. Luz, *Mol. Phys.* **27,** 1345 (1974).
5. T. E. Bull, S. Forsén, and D. L. Turner, *J. Chem. Phys.* **70,** 3106 (1979).
6. J. Carlsson, S. Sjöberg, and B. S. Larsson, *Acta Oncol.* **31,** 803 (1992).
7. F. DeLuca, R. Campanella, A. Bifone, and B. Maraviglia, *Chem. Phys. Lett.* **186,** 303 (1991).
8. F. DeLuca, G. Raza, and B. Maraviglia, *J. Magn. Reson. A* **107,** 243 (1994).
9. P. Bendel, J. Zilberstein, and Y. Salomon, *Magn. Reson. Med.* **32,** 170 (1994).
10. P. Bendel, *J. Magn. Reson. A* **117,** 143 (1995).
11. A. Abragam, ''Principles of Nuclear Magnetism,'' Chaps. VIII, X, Oxford Science, New York (1989).
12. B. Halle and H. Wennerström, *J. Magn. Reson.* **44,** 89 (1981).
13. P. Bendel, A. Frantz, J. Zilberstein, G. W. Kabalka, and Y. Salomon, *Magn. Reson. Med.,* in press (1998).
14. A. J. Leffler, *J. Chem. Phys.* **81,** 2574 (1984).
15. A. Lötz and J. Voigtländer, *J. Chem. Phys.* **85,** 3136 (1986).
16. B. H. Ruessink and C. MacLean, *J. Chem. Phys.* **85,** 3217 (1986).
17. Y. Hiyama, L. G. Butler, and T. L. Brown, *J. Magn. Reson.* **65,** 472 (1985).
18. W. N. Lipscomb, ''Boron Hydrides,'' Benjamin, Elmsford, NY (1963).